RSC Advances

PAPER

Cite this: *RSC Adv.*, 2015, **5**, 72849

Bio-green synthesis of Ni-doped tin oxide nanoparticles and its influence on gas sensing properties

Ketan P. Gattu,[a] Kalyani Ghule,[a] Anil A. Kashale,[a] V. B. Patil,[b] D. M. Phase,[c] R. S. Mane,[d] S. H. Han,[d] Ramphal Sharma[a] and Anil Vithal Ghule*[ae]

Received 10th July 2015
Accepted 12th August 2015

DOI: 10.1039/c5ra13513c

www.rsc.org/advances

Considering the potential applications of transition metal doped nanostructured materials and the advantages of novel, cost-effective and environmentally friendly biosynthesis methods, Ni-doped SnO_2 nanomaterials have been synthesized using remnant water (ideally kitchen waste) collected from soaked Bengal gram bean (*Cicer arietinum* L.) extract. The structural and optical properties of the Ni-doped SnO_2 nanostructures were studied using various techniques such as UV/visible spectroscopy, FT-IR spectroscopy, X-ray powder diffraction (XRD), field-emission scanning electron microscopy (FE-SEM) and transmission electron microscopy (TEM). The SEM and TEM images and the XRD results of the biosynthesized Ni–SnO_2 nanoparticles reveal a uniform size distribution with an average size of 6 nm and confirmed the formation of a rutile structure with the space group (*P*42/*mnm*) and the nanocrystalline nature of the products with a spherical morphology. Subsequently, Ni-doped biosynthesized SnO_2 nanoparticles were coated onto a glass substrate using the doctor blade method to form thin films. The NO_2 sensing properties of the materials have been studied in comparison with other gases. The reported gas sensing results are promising, which suggest that the Ni-dopant is a promising noble metal additive to fabricate low cost SnO_2 based sensors.

Introduction

As an n-type semiconductor, SnO_2 has been extensively studied for various applications, including gas sensors,[1–5] transparent conducting electrodes,[6,7] catalyst support,[8–10] Li-ion battery anode materials[11,12] *etc.* Among these applications of SnO_2, gas sensor applications have been widely explored. A gas sensor is generally characterized by its speed (response–recovery time), selectivity and sensitivity,[13] among which, the sensitivity is important, because higher sensitivity usually means potential sensing ability for detection of gas at a low concentration level. Among various toxic gases, nitrogen dioxide (NO_2) gas is well known as an irritant gas that can cause respiratory infections, photochemical smog, acid rain[14] and it is harmful to human health and life. Thus, it is imperative to develop an applicable sensor for detecting NO_2 gas. With this motivation, extensive efforts have been focused on improving sensor sensitivity towards NO_2 gas. Studies have proved that the properties and performances of SnO_2-based devices are dramatically influenced by structural features. Therefore, most attention has been paid to the synthesis of nanostructured SnO_2 materials with the intension of tuning their properties for selectivity and sensitivity. 1D SnO_2 nanorods,[15] SnO_2 nanosheets,[16] SnO_2 nanoflowers,[17] SnO_2 hollow spheres,[18] 3D porous flower-like SnO_2,[19] microporous Sn–SnO_2/carbon heterostructures,[20] SnO_2–carbon composite nanotubes,[21] hollow porous SnO_2 microcubes[22] *etc.* are a few different forms of SnO_2 nanostructures used in gas sensors.

Apart from this, one of the most important methods for modifying the materials is the introduction of dopants into the host system. Numerous experimental investigations have been performed to improve the responses of the sensors *via* introducing various dopants of either metal oxides[23,24] or noble metals (Pd, Au, Pt, and Ag)[25–27] considering the formation of p–n junctions or the catalytic activity of noble metals. Although noble metal additives have been proven to be very effective for improving sensor performance, their high cost restricts their potential scope for practical applications. Thus, as an economic substitute, SnO_2 doped with transition metal ions such as Co, Mn, Fe, Ni, and Cr has been explored to serve as a sensitizer to decrease the synthetic cost of sensor materials while improving their sensitivity. These dopants cause smaller SnO_2 nanostructure sizes and promote stabilization of their surface. Among the dopants, Ni is of special interest because of its capability for grain growth inhibition within the SnO_2 matrix.[28] Thus, with a

[a]*Department of Nanotechnology, Dr Babasaheb Ambedkar Marathwada University, Aurangabad 431004, Maharashtra, India*
[b]*School of Physical Sciences, Solapur University, Solapur 413255, MS, India*
[c]*UGC-DAE-Consortium of Scientific Research, Indore, M.P, India*
[d]*Department of Chemistry, Hanyang University, Seoul 133-791, Republic of Korea*
[e]*Department of Chemistry, Shivaji University, Kolhapur 416004, Maharashtra, India. E-mail: anighule@gmail.com*

need for a simple, economic and room temperature operated SnO_2 gas sensor, here in this work, we present a novel sensor material of Ni-doped SnO_2 nanoparticles biosynthesized by a completely green approach using remnant water (ideally kitchen waste) collected from soaked Bengal gram beans (*Cicer arietinum* L.). The natural bio-molecule present in the extract which is responsible for biosynthesis of the SnO_2 nanoparticles was found to be pectin. Pectin is a complex polysaccharide that is present in most primary cell walls. It is a natural part of the human diet, but does not contribute significantly to nutrition.[29] Pectin is commonly used in the food industry as a gelling and stabilizing agent, as pectin molecules can bind some organic and inorganic materials *via* molecular interactions, thus finding a use in targeted drug delivery.[30]

Here, in this work, the gas sensing properties of biosynthesized Ni-doped SnO_2 for NO_2 gas and the concentration-dependent behaviours of the sensors to NO_2 are investigated. As well as this, the gas sensing properties of Ni doped SnO_2 for NO_2 gas, are compared with its sensing of other gases like NH_3, LPG and H_2S.

Experimental

In a typical synthesis of Ni-doped tin oxide nanoparticles, 20 g of dry Bengal gram beans (*Cicer arietinum* L.) were soaked in 100 mL of DI water for 6 h at room temperature. Thereafter, the soaked seeds were removed and the extract was filtered using a glass-fiber filter (GF/F) to be free from particulate matter. 10 mL of an aqueous $SnCl_4$ (0.01 M) solution was added to 10 mL of the gram bean extract and diluted to 50 mL. To this solution, an appropriate amount of $NiCl_2 \cdot 6H_2O$ was added to 5 wt% doping. The solution was centrifuged and the powder so obtained was calcined at 600 °C to remove the organic contaminants. This powder was then coated onto the glass substrates to form thin films using the doctor blade method, annealed at 250 °C and was used for further characterizations and gas sensing applications. The Ni-doped SnO_2 nanoparticles so produced were characterized for their preliminary structural and morphological properties. Gas sensing properties of the biosynthesized Ni-doped SnO_2 nanoparticle thin film was studied in detail and its sensitivity for NO_2 gas was investigated in this work. The gas sensing properties of the biosynthesized Ni-doped SnO_2 nanoparticle thin film is also investigated for different gases like NH_3, LPG and H_2S. For better comparison of the NO_2 gas sensing properties of the biosynthesized Ni-doped SnO_2, both pure SnO_2 and Ni-doped SnO_2 nanoparticles were synthesized using a chemical method (sol–gel) as mentioned elsewhere[31] and their NO_2 gas sensing properties were explored.

The biosynthesized nanocrystalline SnO_2 and the Ni-doped SnO_2 nanoparticles were investigated using X-ray diffraction (XRD). The XRD spectra of SnO_2 and Ni-doped SnO_2 nanoparticles (powder form) were recorded using a Bruker D8 Advance X-ray diffractometer. The X-rays were produced using a sealed tube and their wavelength was 0.154 nm (Cu Kα_1 radiation). The X-rays were detected using a fast counting detector based on silicon strip technology (Bruker LynxEye detector). The Ni-doped SnO_2 nanoparticles were sputter coated with platinum to avoid charging effects prior to their characterization using scanning electron microscopy (SEM, JEOL, Japan). On the other hand, the ultrasonically dispersed biosynthesized Ni-doped SnO_2 nanoparticles were drop-coated onto the lacey carbon coated Cu grid and dried prior to TEM analysis using a field emission transmission electron microscope (FE-TEM Tecnai G2 20). FTIR spectra were recorded using FTIR (CARRY 600Z series, Japan) to investigate the characteristics of the functional group of the samples. The optical studies were performed using a Labindia UV-Vis Spectrophotometer 3092.

The thin films of both chemically and biosynthesized, pure and Ni-doped SnO_2 nanoparticles were tested for NO_2 gas sensing. Electrical contacts of silver paste separated by 1 mm were deposited on Ni-doped SnO_2 thin films. The sensor was mounted upside down in a stainless steel test chamber (volume: 250 cm^3). A desired concentration of the test gas in the chamber was achieved by injecting a known quantity of gas using a micro-syringe. A change in resistance of the film as a function of time (response curve) was recorded at an operating temperature of 200 °C for 100, 60 and 20 ppm concentrations of NO_2 gas, which was commercially procured. The response data was acquired by using a computer interfaced 6514 Programmable Electrometer. The recovery of the sensor was recorded by exposing the sensor to air. From the response curves, the sensitivity (S) was calculated using the relation:

$$S(\%) = (R_g - R_a)/R_a \times 100\%$$

where R_a and R_g are resistances in air and test gas (NO_2), respectively.[32–34] Response and recovery times were defined as the times needed for 90% total resistance change on exposure to gas and air, respectively.

Results and discussion

Crystallography

The representative powder X-ray diffraction patterns of pure and Ni-doped SnO_2 (5 wt%) samples are shown in Fig. 1. The diffraction peaks in the spectra were indexed to the rutile phase of the SnO_2 and the lattice parameters were calculated to be $a = 4.78$ Å and $c = 3.21$ Å, which is consistent with the literature values ($a = 4.775$ Å, $c = 3.199$ Å, JCPDS no. 77-0447), belonging to the space group of $P42/mnm$. No peaks due to the metallic tin, NiO, Ni or any other Sn based oxide or hydroxide were observed, indicating the high purity of the final product. There have been reports of the occurrence of traces of NiO in the Ni doped SnO_2 for an excessive dopant concentration of 50 wt% Ni.[35] In the present study, we have used only 5 wt% Ni as the dopant. Thus, the Ni doped SnO_2 can be expected to be phase pure. The average crystallite sizes of the pure and Ni-doped SnO_2 nanoparticles were determined from XRD peaks by using Scherrer's formula $D = K\lambda/\beta \cos\theta$ and noted to be ~11 nm and 6 nm, respectively, where K is the Scherrer's constant ($K = 0.9$), λ is the wavelength of the incident X-rays and β is the full width at half maximum of the XRD peaks expressed in radians. It is known that for a tetragonal structure, the lattice parameters can be calculated by

$$d_{hkl} = \frac{1}{\sqrt{\frac{h^2 + k^2}{a^2} + \frac{l^2}{c^2}}} \quad (1)$$

where h, k, l are all integers, (hkl) is the lattice plane index and a and c are lattice constants.

There is no significant change in the lattice parameters and cell volume, possibly due to the nearly equal size of the dopant Ni ion (0.69 Å) with that of the host ion Sn (0.71 Å). However, upon doping with Ni a pronounced broadening of diffraction peaks is observed. This can be attributed to the decrease of particle size on doping of SnO_2 with Ni through the formation of a Ni–Sn solid solution and/or to the induced microstrain.[36]

Scanning electron microscopy

The surface morphologies of the biosynthesized SnO_2 and Ni-doped SnO_2 nanoparticles were examined by SEM. Fig. 2 shows the micrograph of pure and Ni-doped SnO_2 nanoparticles calcined at 600 °C demonstrating spherical shaped nanoparticles with a narrow size distribution. However, to further confirm the actual size of the SnO_2 nanoparticles, TEM analysis was also employed.

Transmission electron microscopy

TEM studies indicated that both the pristine and Ni-doped SnO_2 (calcined at 600 °C) formed spherical nanoparticles and that the particle sizes decreased due to Ni doping. Fig. 3a shows the representative TEM image of pristine SnO_2 nanoparticles, while Fig. 3b shows the representative TEM image of Ni-doped SnO_2 nanoparticles, calcined at 600 °C. The particles were observed to be monodispersed and the size was noted to be ~11 nm for pure and ~6 nm for Ni doped nanoparticles, showing a narrow size distribution. Interestingly, no aggregation of SnO_2 nanoparticles was observed and the connected crystallites of ~6 nm formed a random network. Selected area electron diffraction (SAED) patterns (insets in Fig. 3a and b) were obtained to investigate the crystallinity. It is observed that the SAED pattern obtained from the nanoparticles showed a ring like pattern, which confirms the polycrystalline nature of the bio-synthesized nanoparticles. It clearly indicates the growth of nanoparticles along the 110, 200, 211 planes (inset in Fig. 3b), which is in agreement with the XRD data. The particle size distribution histograms of pure and Ni-doped biosynthesized SnO_2 nanoparticles calcined at 600 °C are shown in Fig. 3c and d, respectively, demonstrating the average size of the particles.

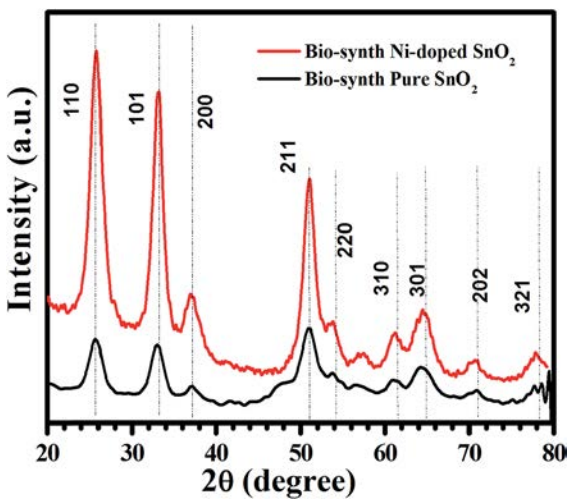

Fig. 1 Representative XRD spectra of pure and Ni-doped bio-synthesized SnO_2 nanoparticles calcined at 600 °C.

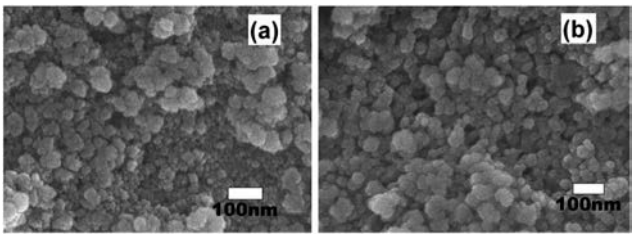

Fig. 2 Representative FE-SEM image of (a) biosynthesized pure SnO_2 nanoparticles and (b) biosynthesized Ni-doped SnO_2 nanoparticles calcined at 600 °C.

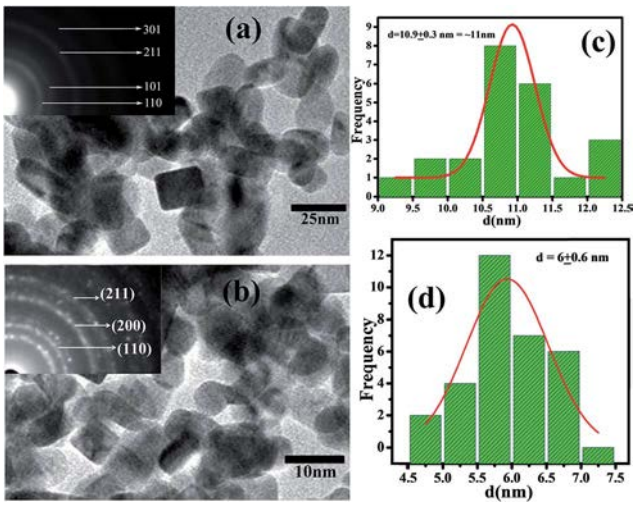

Fig. 3 Representative TEM images of (a) biosynthesized pure SnO_2 nanoparticles (b) biosynthesized Ni-doped SnO_2 nanoparticles calcined at 600 °C. The insets show corresponding SAED patterns. Particle size distribution histogram plots of (c) biosynthesized pure SnO_2 nanoparticles and (d) biosynthesized Ni-doped SnO_2 nanoparticles.

Fourier transform infrared spectroscopy (FTIR)

Room temperature FTIR spectra of drop casted gram bean extract, the as prepared Ni-doped SnO_2 and Ni-doped SnO_2 calcined at 600 °C are shown in Fig. 4. The FTIR spectra of the extract resembles the IR spectra for pectin present in the extract, and thus an obvious absorption peak at about 514 cm^{-1} can be found for the pectin–SnO_2 composite sample; this is a typical IR absorption peak originating from the stretching mode of the Sn–OH bond. The remaining peaks in the pectin–SnO_2 composite are induced by pectin, which is confirmed by

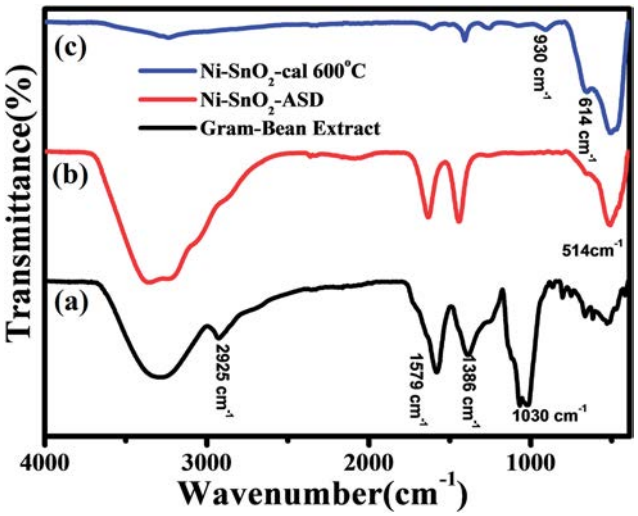

Fig. 4 FTIR spectra of (a) gram bean extract (b) as prepared Ni-doped SnO_2 nanoparticles and (c) Ni-doped SnO_2 nanoparticles calcined at 600 °C.

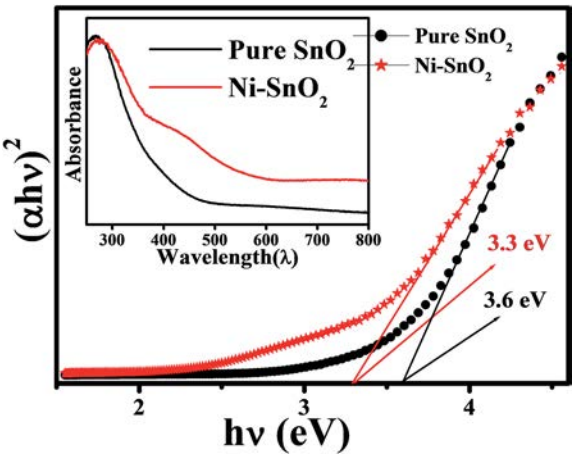

Fig. 6 Band-gap and UV-Vis spectra of pure SnO_2 nanoparticles and Ni-doped SnO_2 nanoparticles calcined at 600 °C.

comparing the IR spectrum of the composite with that of the pectin.[37] The peak at 1030 cm^{-1} is assigned to the C=O or C=C double bond of pectin. The absorption peaks at 1386 and 1579 cm^{-1} are related to stretching bands of the COO^- groups of pectin. It is found that the intensities of the peak around 2925 cm^{-1} (induced by the carboxyl and CH_2 groups of pectin) can be attributed to the pectin–SnO_2 composite and are obviously weaker than that for pectin. This may originate from the participation of COO^- and CH_2 groups in a hydrogen bond system, which stabilizes the pectin conformation in a solid state. The above results indicate that the final product is a true composite of pectin and SnO_2. The pectin peaks were not removed even after washing the sample repeatedly, suggesting that the interactions between pectin and SnO_2 are strong. The peak at around 614–930 cm^{-1}, which refers to Sn–O stretching modes of Sn–O–Sn, appeared even after calcination at 600 °C.

From the synthesis mechanism summarized in Fig. 5, we can conclude that, when gram beans are soaked in de-ionised water, autolysis of the cell wall occurs, which results in the release of pectin molecules in the extract.[38,39] These molecules have a tendency to bind metal ions.[40] Thus, when tin chloride is added to the extract, the tin ions get bound to the pectin molecules as shown in Fig. 5. As the pH of the solution is increased, this tin-hydroxide–pectin gel shrinks[30] and inhibits the further growth of the nanoparticles. Subsequently, when it is calcined, we get very small sized nanoparticles with a narrow size distribution.

Absorbance and band gap of Ni-doped SnO_2

Absorption spectroscopy is a powerful, non-destructive technique to explore the optical properties of semiconducting nanoparticles. The absorption spectra of pure and Ni doped SnO_2 nanoparticles are shown in Fig. 6. The absorbance is expected to depend on several factors, such as band gap, oxygen deficiency, surface roughness and impurity centres. The absorbance spectra show an ultraviolet cut-off at around 250–290 nm, which can be attributed to the photo-excitation of electrons from the valence band to the conduction band.

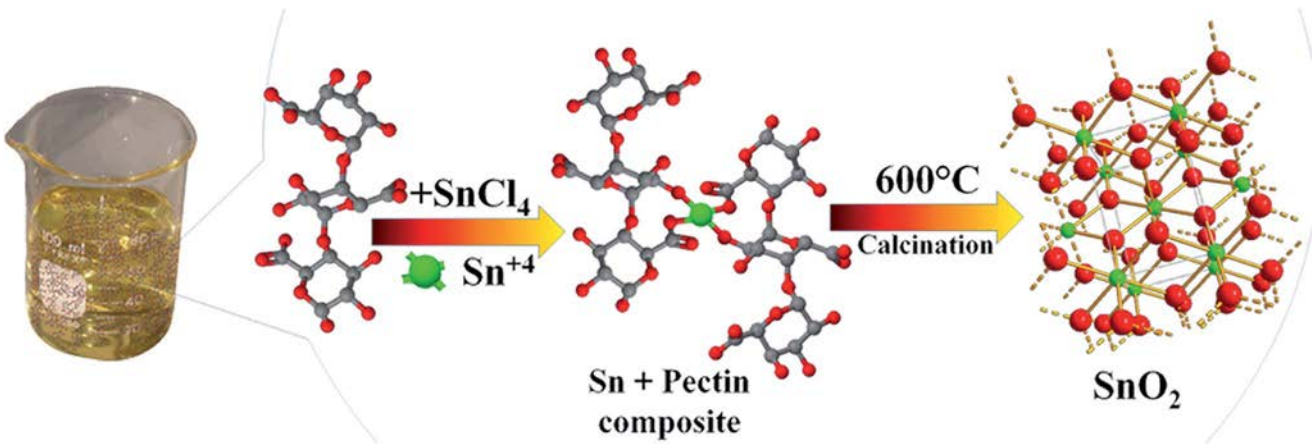

Fig. 5 Schematic representation of the biosynthesis mechanism using gram bean extract.

Table 1 Comparison of gas-sensing characteristics of the sensing material in the present work with those reported in the literature

Sr. no.	Sensing material	Synthesis method	Analyte gas	Gas concentration	Operating temperature	Response	Ref. no.
1	SnO_2 nanobelts	Carbothermal reduction method	NO_2	100 ppb	200 °C	~2	42
2	(rGO–CNT–SnO_2)	Hydrothermal method	NO_2	5 ppm	RT	2.53	43
3	SnO_2 nanowire	Thermal evaporation method.	NO_2	10 ppm	100 °C	117	44
4	Ag functionalized SnO_2 microrods	Vapor–liquid–solid (VLS) method	NO_2	10 ppm	200 °C	2700	45
5	Flower-like In_2O_3	Solvothermal	NO_2	0.2 ppm	140 °C	41.1	46
6	Graphene modified by ZnO	CVD, ALD	NO_2	10 ppm	200 °C	38	47
7	Hollow In_2O_3 microspheres	Hydrothermal	NO_2	500 ppb	80 °C	737.8	48
8	Ni-doped SnO_2 nanoparticles	Gram bean extract mediated synthesis	NO_2	100 ppm	200 °C	40	This work

The Tauc relation is used to calculate the band gap: $\alpha h\nu = A(h\nu - E_g)^n$ where α is the absorption coefficient, A is a constant and $n = 1/2$ for a direct band gap semiconductor. An extrapolation of the linear region of a plot of $(\alpha h\nu)^2$ *vs.* $h\nu$ gives the value of the optical band gap E_g. The measured band gap was found to be 3.6 eV for undoped SnO_2 nanoparticles and 3.3 eV for Ni-doped SnO_2. The bandgap of the pure SnO_2 nanoparticles is in agreement with the reported value. However, on doping with nickel, the band gap energy decreases even though the particle size decreases. This is in contrast to the normal phenomenon of quantum confinement. A similar phenomenon was observed by Ahmed *et al.*[41] for samples containing 5% Ni concentration, where the SnO_2–SnO_{2-x} alloying effect was considered responsible for the band gap narrowing effect.

Gas sensing

Gas-sensing behaviours of the Ni-doped SnO_2 sensor were explored after NO_2 gas injection. The response–recovery properties of semiconducting oxide gas sensors depend on the operating temperature and gas concentrations. Table 1 shows a comparison of the NO_2 gas-sensing characteristics of sensing material in the present work and those reported in the literature. From the table, we observe that for a higher response at a lower concentration, sophisticated synthesis methods need to be used. Meanwhile in the present work a simple, economic and eco-friendly biosynthesis method is used. For better comparison of the gas sensing properties of the biosynthesized Ni doped SnO_2, the gas sensing properties of both pure and nickel doped biosynthesized SnO_2 and both pure and nickel doped chemically synthesized (sol–gel method) SnO_2 were studied and their respective response curves for 100 ppm NO_2 gas at 200 °C are shown in Fig. 7. The resulting gas responses along with response and recovery time are summarized in Table 2. The sensor resistance increased when exposed to NO_2 gas and consequently recovered to its original value on removal of the NO_2 gas. From Fig. 7 we can clearly see that the response was relatively higher for biosynthesized Ni-doped SnO_2 compared to chemically synthesized Ni-doped SnO_2. The sensor response for chemically synthesized SnO_2 was similar to the reported value.[31] Furthermore, we observe that the sensor response increased with Ni doping for both the samples. This may be due to the reduction of particle size upon Ni doping,[36] which resulted in an increased surface area for adsorption of NO_2 gas. The inset in Fig. 7 shows a decrease in response time and increase in recovery time with an increase in gas concentration for biosynthesized Ni–SnO_2. The decrease in response time may be due to the large availability of vacant sites on the film for gas adsorption and the increase in the recovery time may be due to the heavier nature of NO_2 and the reaction products which are not leaving the interface immediately after the reaction, resulting in a decrease in desorption rate.[31]

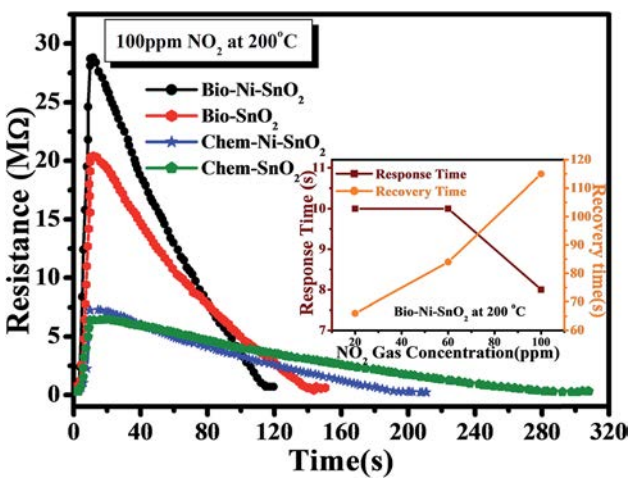

Fig. 7 Gas sensitivity for chemically and biosynthesized pure and Ni-doped SnO_2 nanoparticle thin films. Inset shows variation in the response and recovery time of the Ni-doped SnO_2 sensors with varying NO_2 gas concentration.

It is well known that the NO_2 sensing mechanism of SnO_2 depends on the surface oxygen adsorbed on the SnO_2 nanoparticle surface. The sensing mechanism involves adsorption of oxygen species on the surface of tin oxide nanoparticles, which causes the removal of electrons, and thus, causes an increase in the potential barrier at the grain boundaries. The gas molecules

Table 2 Summarised responses, response time and recovery time

Sr. no.	Sensing material NO_2 conc.	Response time (s) 20 ppm	60 ppm	100 ppm	Recovery time (s) 20 ppm	60 ppm	100 ppm	Response
1	Chem-SnO_2	26	20	14	145	225	310	20
2	Chem-Ni–SnO_2	20	15	10	145	172	200	23
3	Bio-SnO_2	20	15	10	90	120	145	28
4	Bio-Ni–SnO_2	10	10	8	66	84	115	40

interact with the oxygen species and produce a notable change in the electronic property of the material. Thus, the density of oxygen species on the surface defines the rate of reaction and the catalytic properties. NO_2 is an oxidizing gas with an electron affinity much higher than oxygen (0.48 eV); NO_2 can interact with SnO_2 by trapping electrons directly through the surface oxygen ions thereby forming new surface electron acceptor levels.[49,50]

$$O_2\ \text{gas} \xrightarrow{\text{Ni–SnO}_2\text{+ air}} O_2(\text{ads})$$

$$O_2(\text{ads}) + e^- \xrightarrow{\text{Ni–SnO}_2\text{+ air}} O_2^-(\text{ads})$$

$$O_2^-(\text{ads}) + e^- \xrightarrow{\text{Ni–SnO}_2\text{+ air}} 2O^-(\text{ads})$$

$$NO_2(\text{gas}) \leftrightarrow NO_2(\text{ads})$$

$$NO_2(\text{ads}) + O_2^-(\text{ads}) + 2e^- \leftrightarrow NO_2^-(\text{ads}) + 2O^-(\text{ads}) \quad (2)$$

To explore further the picture of the NO_2 sensing mechanism, we plotted the response at different NO_2 gas concentrations as shown in Fig. 8. The inset shows a power–law relationship of response (S) and NO_2 gas concentration.

The power exponent value (m) was fitted as $m = 0.48566$. These exponent values depend on the final adsorbed species at the surface; when the adsorbed species are NO_2^- or O^-, the exponent values for both are 1. In the case of $2O^-$, the exponent value is 0.5.[51] Thus, our results indicate that the electrons in SnO_2 will transfer adsorbed species to the new surface due to NO_2 adsorption, increasing the surface potential barrier of SnO_2 and thus causing its resistance to increase.

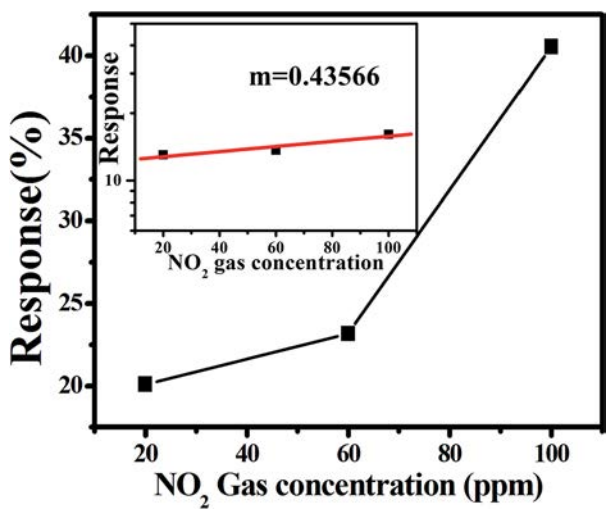

Fig. 8 Gas response curve for Ni-doped SnO_2 nanoparticle thin films for different concentrations of NO_2 gas. Inset shows log(response(S)) *vs.* gas concentration plot.

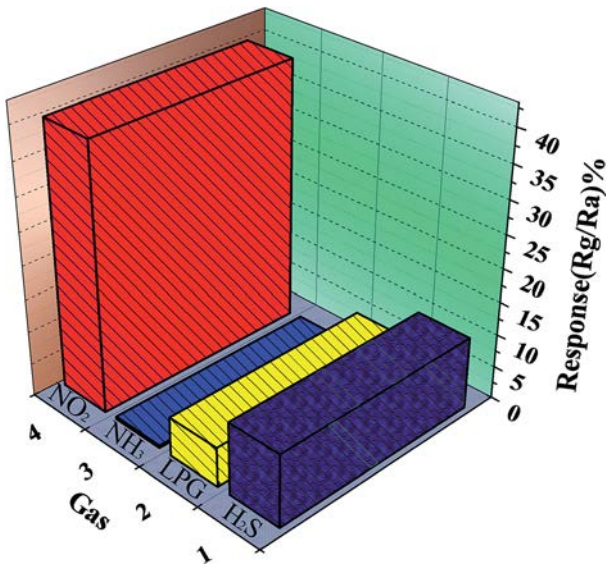

Fig. 9 Gas selectivity for the Ni-doped SnO_2 sensor for different gases (H_2S, LPG, NH_3 and NO_2) of 100 ppm concentration.

Selectivity was studied as another sensor parameter. The responses of Ni-doped SnO_2 sensors towards a variety of flammable, toxic and corrosive gases including H_2S, LPG, NH_3 and NO_2 of 100 ppm at the optimal operating temperature of NO_2 (200 °C) were explored to evaluate their selectivity. Fig. 9 shows that the gas sensor of 'Ni-doped SnO_2' exhibited excellent selectivity to NO_2 gas when compared to other gases. The results suggest that the Ni-doped SnO_2 thin film sensor can be fabricated to monitor highly toxic NO_2 in polluted air.

Conclusions

Ni-doped SnO_2 nanoparticles were successfully biosynthesized using remnant water (ideally kitchen waste) collected from soaked Bengal gram beans (*Cicer arietinum* L.) making it a greener approach. This procedure resulted in the formation of well dispersed nanoparticles with a narrow size distribution and with a size of ~6 nm. This was confirmed from XRD and TEM analyses. The SAED pattern confirmed the polycrystalline nature of SnO_2 nanoparticles. FE-SEM could confirm the narrow

size distribution of the Ni-doped SnO_2 nanoparticles. Gas sensors based on the Ni-doped SnO_2 showed a gas response of 40 at 100 ppm of NO_2 gas, which is a promising result for the biosynthesized Ni-doped SnO_2 nanoparticle thin films for gas sensing applications and can be attributed to the small size and uniform distribution of Ni-doped SnO_2 nanoparticles within the thin film. The synthesis method described in this work is facile and versatile, providing opportunities to control the morphology of various other semiconducting metal oxides, with particular promise for application in gas sensors.

Acknowledgements

The authors are thankful to the UGC-DAE Consortium for Scientific Research, Indore (Project Ref. No: CSR-I/CRS-48/48) and UGC, New Delhi (F. No. 41-370/2012 (SR)) for the financial support. We are also thankful to the Department of Nanotechnology, Dr B. A. M. University for providing the laboratory facility.

References

1 S. Maeng, S.-W. Kim, D.-H. Lee, S.-E. Moon, K.-C. Kim and A. Maiti, *ACS Appl. Mater. Interfaces*, 2013, **6**, 357–363.
2 S. Park, S. An, S. Park, C. Jin, W. Lee and C. Lee, *Appl. Phys. A*, 2013, **110**, 471–477.
3 B.-G. Kim, D.-G. Lim, J.-H. Park, Y.-J. Choi and J.-G. Park, *Appl. Surf. Sci.*, 2011, **257**, 4715–4718.
4 H. Zhang, J. Feng, T. Fei, S. Liu and T. Zhang, *Sens. Actuators, B*, 2014, **190**, 472–478.
5 K. P. Gattu, K. Ghule, A. A. Kashale, R. S. Mane, R. Sharma, D. M. Phase, S. H. Han and A. V. Ghule, *Curr. Nanosci.*, 2015, **11**, 253–260.
6 K. Ellmer, *Nat. Photonics*, 2012, **6**, 808–816.
7 H. Kim, R. C. Y. Auyeung and A. Pique, *Thin Solid Films*, 2008, **516**, 5052–5056.
8 Z. Liu, D. Fu, F. Liu, G. Han, C. Liu, Y. Chang, Y. Xiao, M. Li and S. Li, *Carbon*, 2014, **70**, 295–307.
9 S. Sago, A. B. Suryamas, G. M. Anilkumar, T. Ogi and K. Okuyama, *Mater. Lett.*, 2013, **105**, 202–205.
10 M. N. Alaya and M. A. Rabah, *J. Alloys Compd.*, 2013, **575**, 285–291.
11 L. Wang, D. Wang, Z. Dong, F. Zhang and J. Jin, *Small*, 2014, **10**, 998–1007.
12 J.-Y. Lin, M.-H. Chou and Y.-C. Kuo, *J. Alloys Compd.*, 2014, **589**, 472–478.
13 J. Zhang, S. Wang, Y. Wang, Y. Wang, B. Zhu, H. Xia, X. Guo, S. Zhang, W. Huang and S. Wu, *Sens. Actuators, B*, 2009, **135**, 610–617.
14 J.-R. Zhang, L. Gao and L.-X. Gu, *Chin. J. Inorg. Chem.*, 2006, **22**, 2001–2004.
15 S. Wang, J. Yang, H. Zhang, Y. Wang, X. Gao, L. Wang and Z. Zhu, *Sens. Actuators, B*, 2015, **207**, 83–89.
16 T. Tao, L. He, J. Li and Y. Zhang, *Mater. Lett.*, 2015, **138**, 45–47.
17 W. X. Jin, S. Y. Ma, A. M. Sun, J. Luo, L. Cheng, W. Q. Li, Z. Z. Tie, X. H. Jiang and T. T. Wang, *Mater. Lett.*, 2015, **143**, 283–286.
18 Y. H. Cho, X. Liang, Y. C. Kang and J.-H. Lee, *Sens. Actuators, B*, 2015, **207**, 330–337.
19 L. Cheng, S. Y. Ma, T. T. Wang and J. Luo, *Mater. Lett.*, 2015, **143**, 84–87.
20 S. Yan and Q. Wu, *Sens. Actuators, B*, 2014, **205**, 329–337.
21 F. Mendoza, D. M. Hernández, V. Makarov, E. Febus, B. R. Weiner and G. Morell, *Sens. Actuators, B*, 2014, **190**, 227–233.
22 J. Huang, L. Wang, C. Gu and J.-J. Shim, *Mater. Lett.*, 2014, **136**, 371–374.
23 G. Zhang and M. L. Liu, *Sens. Actuators, B*, 2000, **69**, 144–152.
24 A. Chowdhuri, V. Gupta and K. Sreenivas, *Sens. Actuators, B*, 2003, **93**, 572–579.
25 A. Kolmakov, D. O. Klenov, Y. Lilach, S. Stemmer and M. Moskovits, *Nano Lett.*, 2005, **5**, 667–673.
26 Y.-S. Shim, H. G. Moon, D. H. Kim, L. Zhang, S.-J. Yoon, Y. S. Yoon, C.-Y. Kang and H. W. Jang, *RSC Adv.*, 2013, **3**, 10452–10459.
27 E. Y. Sevastyanov, N. K. Maksimova, V. A. Novikov, F. V. Rudov, N. V. Sergeychenko and E. V. Chernikov, *Semiconductors*, 2012, **46**, 801–809.
28 K. Jain, R. P. Pant and S. T. Lakshmikumar, *Sens. Actuators, B*, 2006, **113**, 823–829.
29 Pectin, https://en.wikipedia.org/w/index.php?title=Pectin&oldid=674518015.
30 T. F. Vandamme, A. Lenourry, C. Charrueau and J. Chaumeil, *Carbohydr. Polym.*, 2002, **48**, 219–231.
31 G. D. Khuspe, R. D. Sakhare, S. T. Navale, M. A. Chougule, Y. D. Kolekar, R. N. Mulik, R. C. Pawar, C. S. Lee and V. B. Patil, *Ceram. Int.*, 2013, **39**, 8673–8679.
32 G. D. Khuspe, S. T. Navale, D. K. Bandgar, R. D. Sakhare, M. A. Chougule and V. B. Patil, *Electron. Mater. Lett.*, 2014, **10**, 191–197.
33 M. A. Chougule, S. R. Nalage, S. Sen and V. B. Patil, *J. Exp. Nanosci.*, 2012, **9**, 482–490.
34 S. T. Navale, A. T. Mane, M. A. Chougule, N. M. Shinde, J. Kim and V. B. Patil, *RSC Adv.*, 2014, **4**, 44547–44554.
35 M. P. Hidalgo Falla, H. E. M. Peres and F. J. Ramirez-Fernandez, *Phys. Status Solidi C*, 2004, **1**, S112–S115.
36 N. Lavanya, S. Radhakrishnan and C. Sekar, *Biosens. Bioelectron.*, 2012, **36**, 41–47.
37 L. Shi and S. Gunasekaran, *Nanoscale Res. Lett.*, 2008, **3**, 491–495.
38 E. Martinez-Manrique, C. Jacinto-Hernandez, R. Garza-Garcia, A. Campos, E. Moreno and I. Bernal-Lugo, *J. Sci. Food Agric.*, 2011, **91**, 2394–2398.
39 J. M. Sevillano, I. Zarra and J. L. Acebes, *Plant Cell Physiol.*, 1997, **38**, 1259–1263.
40 B. A. McKenna, T. M. Nicholson, J. B. Wehr and N. W. Menzies, *Carbohydr. Res.*, 2010, **345**, 1174–1179.
41 A. S. Ahmed, S. M. Muhamed, M. L. Singla, S. Tabassum, A. H. Naqvi and A. Azam, *J. Lumin.*, 2011, **131**, 1–6.
42 P. H. Suman, A. A. Felix, H. L. Tuller, J. A. Varela and M. O. Orlandi, *Sens. Actuators, B*, 2015, **208**, 122–127.
43 S. Liu, Z. Wang, Y. Zhang, C. Zhang and T. Zhang, *Sens. Actuators, B*, 2015, **211**, 318–324.

44 L. Dang Thi Thanh, D. Nguyen van, T. Ha Minh, T. Do Dang, T. Nguyen Ngoc, V. Phung Thi Hong, H. Nguyen Duc and H. Nguyen van, *J. Mater. Sci.*, 2013, **48**, 7253–7259.
45 S.-W. Choi, A. Katoch, G.-J. Sun, P. Wu and S. S. Kim, *J. Phys. Chem. C*, 2013, **1**, 2834–2841.
46 X. Xu, X. Li, H. Zhang, C. Feng, C. Wang, F. Liu, Y. Sun, P. Sun and G. Lu, *RSC Adv.*, 2015, **5**, 30297–30302.
47 H. Xie, K. Wang, Z. Zhang, X. Zhao, F. Liu and H. Mu, *RSC Adv.*, 2015, **5**, 28030–28037.
48 X. Hu, X. Zhou, B. Wang, P. Sun, X. Li, C. Wang, J. Liu and G. Lu, *RSC Adv.*, 2015, **5**, 4609–4614.
49 B. Ruhland, T. Becker and G. Müller, *Sens. Actuators, B*, 1998, **50**, 85–94.
50 M. Epifani, J. D. Prades, E. Comini, E. Pellicer, M. Avella, P. Siciliano, G. Faglia, A. Cirera, R. Scotti, F. Morazzoni and J. R. Morante, *J. Phys. Chem. C*, 2008, **112**, 19540–19546.
51 A. Gurlo, N. Bârsan, M. Ivanovskaya, U. Weimar and W. Göpel, *Sens. Actuators, B*, 1998, **47**, 92–99.